PAPER

Check for updates

Highly efficient catalytic conversion of 2,5-dimethylfuran and acrylic acid to *para*-xylene over MCM-22 zeolites

Bing Yan,[a] Xu Chen,[a] Guangming Min,[a] Yajing Song,[a] Zhansheng Wang,[a] Jie Huang,[a] Lei Shi,[b] Zonghui Liu [ID][a] and Bing Xue [ID] *[a]

Producing *para*-xylene (PX) by Diels–Alder (D–A) cycloaddition of 2,5-dimethylfuran (DMF) and acrylic acid (AA) was a potential renewable pathway. In this study, MCM-22 zeolites served as catalysts for the D–A cycloaddition reaction, exhibiting significantly higher activity compared to conventional beta and ZSM-5 zeolites. The high activity was demonstrated to be derived mainly from the acid sites located within the pocket structures on the external surface of MCM-22. The rate-determining step for the formation of PX was the dehydration process of the B-acid-catalyzed cycloadduct. The external silanols at the pore entrance of the pocket structure could adsorb the reactants and promote the D–A cycloaddition reaction. The MCM-22(15) catalyst achieved 98% DMF conversion with 88% PX selectivity after 10 h at 190 °C in the D–A cycloaddition reaction.

1. Introduction

As a high-demand chemical, *para*-xylene (PX) was widely applied in producing precursors of multiple polymers.[1–3] The demand for PX has exceeded more than 40 million tons annually in recent years. Traditionally, PX was mainly derived from thermal cracking and catalytic reforming of naphtha.[4,5] Compared to the traditional route, the production of PX by Diels–Alder (D–A) conversion of 2,5-dimethylfuran (DMF) and dienophiles (Scheme 1) was a more sustainable process.[6–8] Usually, acrylic acid (AA), ethylene, and alcohol could be used as the dienophiles in this reaction.[9–11] Among them, AA, as the dienophile, could proceed under mild conditions and achieve an elevated PX yield.
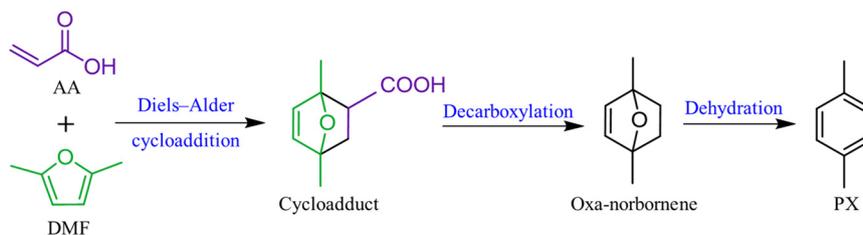
The synthesis of PX through the D–A reaction between DMF and dienophile involves steps such as cycloaddition and dehydration, which require both Brønsted (B) and Lewis (L) acid sites.[13,14] Zeolites, which possess both L and B acid sites and exhibit remarkable hydrothermal stability, have been widely used in the D–A conversion of DMF. Fan *et al.* showed that a 90% yield of PX could be obtained when beta was used to catalyze the conversion of DMF and ethylene at high temperature and pressure.[15] Al-Naji *et al.* reported that beta and Y zeolites showed good catalytic performance for the

conversion of DMF and AA to PX in a continuous flow system.[7] Kim *et al.* found that the yield of PX was only 8.4% in the DMF-to-PX reaction when using pristine ZSM-5 zeolite, and it was up to 75.5% when using mesoporous ZSM-5 zeolite.[16] Many studies have shown that beta and Y zeolites showed significantly higher catalytic activity than ZSM-5.[7,17,18] Besides, beta was considered to exhibit higher selectivity to PX compared to Y zeolite due to its desirable pore size.[19] ZSM-5 exhibits greater difficulty in achieving high selectivity for PX because of its smaller pore size compared to the cycloadduct intermediate. These findings demonstrated that the structure of zeolites influenced not only the mass transfer limitation but also the reaction process during the D–A conversion of DMF.

Adjusting the pore structure of zeolites or selecting the appropriate zeolite topologies can effectively promote the D–A conversion of the DMF. Using mesoporous zeolites synthesized by desilication and dealumination or the mesoscale template route can effectively improve the mass transfer efficiency.[20–22] However, these methods were often accompanied by cumbersome procedures or a decrease in zeolite crystallinity.[23,24] MCM-22 is a lamellar-shaped zeolite characterized by high external surface area and tunable thickness.[25–27] The external surface of MCM-22 features pocket-like pores (0.71 × 0.70 nm), which not only contain many acid sites but also show highly accessible.[28,29] Moreover, the special pocket structure was thought to stabilize the cycloadduct intermediate of D–A conversion of DMF, which could be able to improve the conversion of DMF to PX.[30] In addition, the abundant hydroxyl groups at the pore

[a] Jiangsu Key Laboratory of Advanced Catalytic Materials and Technology, School of Petrochemical Engineering, Changzhou University, Changzhou, Jiangsu 213164, China. E-mail: bingxue@cczu.edu.cn
[b] State Key Laboratory of Fine Chemicals, School of Chemical Engineering, Dalian University of Technology, Dalian 116024, Liaoning, China

This journal is © The Royal Society of Chemistry 2025

Catal. Sci. Technol., 2025, **15**, 6179–6187 | **6179**

Scheme 1 Reaction pathway for PX synthesis from DMF and AA on zeolites.[12]

entrance of the pocket structure may promote the adsorption of polar reactants, thereby enhancing the D–A conversion of DMF.

In this work, MCM-22 zeolites were employed to catalyze DMF and AA to PX. MCM-22 zeolites exhibited superior catalytic performance compared to the commonly used beta and ZSM-5 zeolites. Combining structural analysis, poisoning experiments, kinetic evaluations, and *in situ* FTIR, the superior activity of MCM-22 was studied in detail. In addition, the effects of reaction conditions were also discussed to further understand the D–A conversion of DMF over MCM-22.

2. Experimental section

2.1 Catalyst preparation

MCM-22 zeolites were synthesized *via* a hydrothermal method with the component proportions of $SiO_2 : nAl_2O_3 : 0.5$hexamethyleneimine (HMI) $: 0.05Na_2O : 15H_2O$ ($n = 0.022$, 0.017). The synthesis gels were placed in a Teflon-lined stainless-steel autoclave at 150 °C for 120 h under rotation. The resultant crystals were collected *via* filtration, rinsed with deionized water, and finally dried at 120 °C for 12 h. The final samples were labeled as MCM-22(Px), where x stands for the Si/Al molar ratio. The MCM-22(Px) materials were initially heated under air at 550 °C for 6 h followed by three cycles of ion-exchange treatment using a 1 M NH$_4$Cl aqueous solution maintained at 80 °C. After overnight dehydration in a 120 °C oven, the material underwent a final calcination process at 550 °C for 4 h under air conditions to yield the proton form of the zeolite. The products were designated as MCM-22(x). ZSM-5 (Si/Al = 12.5), beta-25 (Si/Al = 25), and beta-50 (Si/Al = 50) were bought from Nankai University Catalyst Company Limited. Beta-100 (Si/Al = 100) was bought from Shanghai Aladdin Biochemical Technology Company Limited.

MCM-22(15) was loaded with SiO$_2$ to selectively mask cover the acid centers. 0.52 g tetraethyl orthosilicate (TEOS) was first dissolved in 10 mL cyclohexane solution, and then the MCM-22(15) (1 g) sample was dispersed in the mixed solution at 25 °C for 2 h. Subsequently, the suspending liquid was heated to 80 °C to vaporize the cyclohexane. In the final step, the powder underwent calcination at 550 °C for 3 h, yielding the sample designated as SiO$_2$/MCM-22(15), where the weight percentage of SiO$_2$ was 15%.

2.2 Catalytic evaluation

The D–A cycloaddition of the DMF and AA system was established in a Teflon tube with sequential addition of DMF (7.5 mmol), AA (7.5–30 mmol), and varying amounts of catalyst (20–200 mg) along with *n*-heptane (20 mL) and *n*-decane (0.2 mL) serving as the solvent and internal standard, respectively. Then the mixed solution was subjected to thermal treatment at an appropriate temperature under continuous agitation, followed by conducting the reaction under an N$_2$ atmosphere with around 1 MPa reaction pressure. Upon completion of the reaction and subsequent cooling to ambient temperature, the resulting mixture was subjected to gas chromatographic analysis utilizing an FFAP capillary column. For the D–A cycloaddition of the DMF and ethylene system, all parameters remained identical to the procedure described above, except for replacing N$_2$ with ethylene (2 MPa) and removing reactant AA. All the results were tested at the DMF conversion of less than 15% during the kinetic analysis experiments.

In the selective poisoning experiments, 2,6-di-*tert*-butylpyridine (DTB-Py) was used to selectively poison the B acid sites located on the external surface of MCM-22. Specifically, additional amounts of DTB-Py were introduced into the reaction mixture, with subsequent evaluation of their influence on catalytic performance. In addition, the isomerization of 1,3,5-triisopropylbenzene (TPB) was tested to reflect the change in the densities of the acid site on the external surface of zeolites. The isomerization reaction was carried out at 320 °C with a WHSV of TPB at 1.7 min^{-1}.

DMF conversion, product selectivity and yield values were determined by:

$$Conversion_{DMF} = \frac{\sum M_{i,t}}{M_{DMF,t_0}} \times 100\%$$

$$Selectivity_{product} = \frac{M_{i,t}}{\sum M_{i,t}} \times 100\%$$

$$Yield_{product} = Conversion_{DMF} \times Selectivity_{product}$$

where M_i denotes the molar amount of product species i, with t representing the reaction time.

2.3 Catalyst characterization

The physicochemical attributes of the catalysts were probed *via* N$_2$ sorption isotherms, scanning electron microscopy
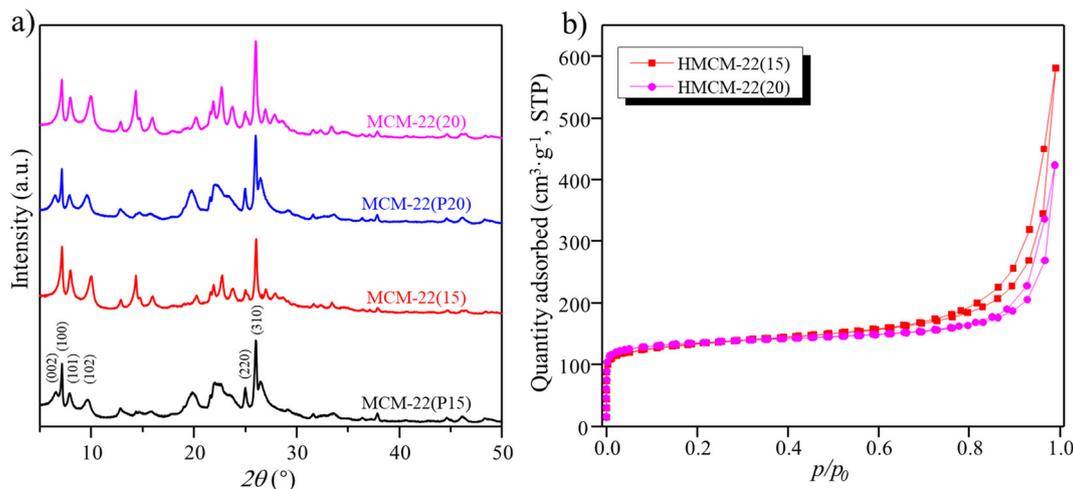
6180 | *Catal. Sci. Technol.*, 2025, **15**, 6179–6187

This journal is © The Royal Society of Chemistry 2025

Fig. 1 (a) XRD patterns of MCM-22(Px) and MCM-22(x); (b) N$_2$ sorption isotherms of MCM-22(x).

(SEM), X-ray diffraction (XRD), inductively coupled plasma optical emission spectroscopy (ICP-OES), temperature-programmed desorption of NH$_3$ (NH$_3$-TPD), and FTIR spectra of pyridine adsorption. The complete experimental processes are delineated within the SI.

3. Results and discussion

3.1 Characterization of catalysts

The XRD patterns (2θ = 5–50°) of MCM-22(P15), MCM-22(15), MCM-22(P20), and MCM-22(20) samples are presented in Fig. 1a. Each of the samples displayed the typical characteristic signals of MWW topology, with no detection of other structural signals. For MCM-22(P15) and MCM-22(P20), the peaks at 6.5°, 7.1°, 9.7°, 22.5°, 25.0°, and 26.0° correspond to the reflections of (002), (100), (101), (102), (220), and (310).[31] When the template was removed, the peak at 6.5° disappeared. This was because the position of the (002) reflection was close to that of the (100) reflection, causing it to be undetected by XRD for the MCM-22(x) samples. Besides, in the 2θ range of 21.5–24.0°, new diffraction signals appeared after template removal, suggesting the terminal Si–OH groups between the single-unit MWW sheets were combined.[32]

The results of N$_2$ adsorption isotherms for MCM-22(15) and MCM-22(20) are shown in Fig. 1b and Table 1. Both MCM-22(15) and MCM-22(20) samples exhibited type I shape of isotherms, indicating they were representative microporous materials. The pore size of MCM-22(15) and MCM-22(20) was concentrated at ~0.5 nm (Fig. S1). The

specific surface area (S_{BET}) for MCM-22(15) and MCM-22(20) was 428 and 413 m^2 g^{-1}, respectively. The micropore surface area (S_{micro}) obtained by the t-plot method for MCM-22(15) and MCM-22(20) was 269 and 302 m^2 g^{-1}, respectively. The difference between S_{BET} and S_{micro} was used to calculate the external surface area (S_{ext}). The S_{ext} of MCM-22(15) and MCM-22(20) was 159 and 111 m^2 g^{-1}, implying an abundant S_{ext} for zeolites to ensure the accessibility of active sites in the catalytic reaction. The micropore volume (V_{micro}) of MCM-22(15) and MCM-22(20) was 0.14 and 0.16 cm^3 g^{-1}, but the total pore volume (V_{total}) was as high as 0.44 and 0.32 cm^3 g^{-1}, respectively. When the value of P/P_0 was higher than 0.9, a sharp increase in adsorption was observed for both MCM-22(15) and MCM-22(20). Therefore, the high V_{total} may be caused by the macropore formed by the stacking of zeolite particles.

Fig. 2 shows the SEM images of MCM-22(15) and MCM-22(20). Both MCM-22(15) and MCM-22(20) showed a lamellar shape with a diameter of 0.5–1 μm and a thickness of less than 100 nm. Compared with MCM-22(P15) and MCM-22(P20) (Fig. S2), the morphology showed almost no change, suggesting calcination has hardly affected the structure of MCM-22 catalysts. Besides, the lamellae of MCM-22 zeolites stack disordered to form many macropores, which was consistent with the N$_2$ adsorption isotherms results.

The NH$_3$-TPD and Py-IR spectra were obtained to characterize the acid properties of MCM-22(15) and MCM-22(20). As shown in Fig. 3a, two desorption peaks at around 230 and 430 °C were attributed to weak and strong

Table 1 Textural parameters of MCM-22(15) and MCM-22(20)

Samples	S_{BET} (m^2 g^{-1})	S_{micro} (m^2 g^{-1})	S_{ext} (m^2 g^{-1})	$V_{total}{}^a$ (cm^3 g^{-1})	$V_{micro}{}^b$ (cm^3 g^{-1})
MCM-22(15)	428	269	159	0.44	0.14
MCM-22(20)	413	302	111	0.32	0.16

^{a} Calculated at P/P_0 = 0.99. ^{b} Calculated from t-plot.

This journal is © The Royal Society of Chemistry 2025

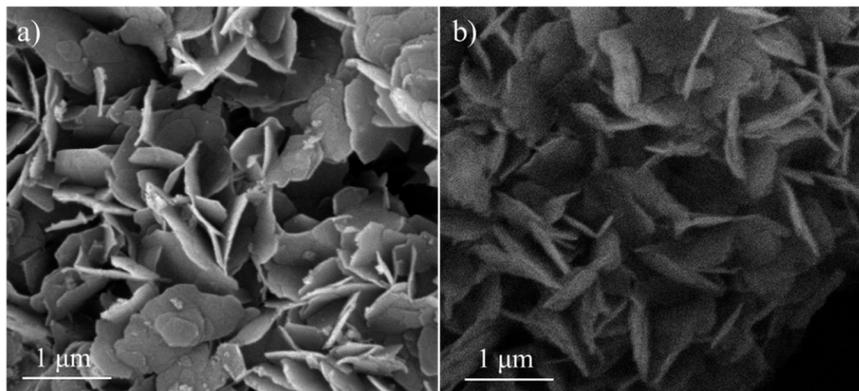Catal. Sci. Technol., 2025, 15, 6179–6187 | 6181

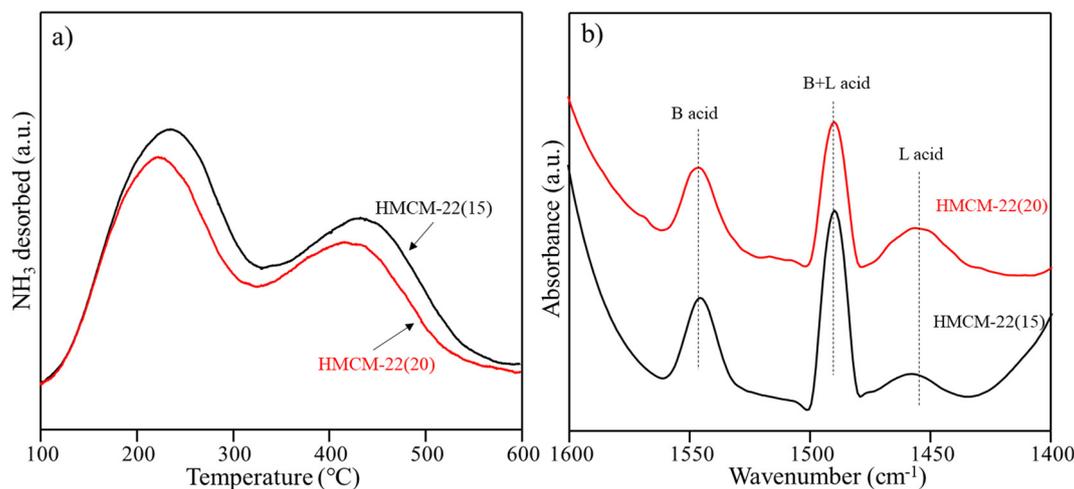**Fig. 2** SEM images of (a) MCM-22(15) and (b) MCM-22(20).

Fig. 3 (a) NH$_3$-TPD profiles, (b) Py-IR spectra for MCM-22(15) and MCM-22(20).

acid sites. The concentrations of acid sites were 520 and 379 µmol g^{-1} determined by the NH$_3$-TPD results. As shown in Fig. 3b, the absorption peaks corresponding to pyridine were observed at 1546 and 1455 cm^{-1}, which were caused by the adsorption of pyridine at the B and L acid sites. Based on the peak area of Py-IR spectra, the ratios of B acid to L acid (B/L) for MCM-22(15) and MCM-22(20) were calculated as 4.0 and 1.3, respectively. This result suggested that MCM-22(15) may have more framework Al species than MCM-22(20).

3.2 Catalytic evaluation

The catalytic performance of MCM-22(20), MCM-22(15), beta-25, beta-50, beta-100, and ZSM-5 is shown in Fig. 4 and Table S2. After reacting at 160 °C for 5 h, the conversion of DMF and PX selectivity were 61% and 68% at 160 °C with 2,5-hexanedione (HDO, 16%), 2,5-dimethylbenzoic acid (DMBA, 10%), and dimethylcyclohexenone (DMCHO, 2%) as the main by-products for the MCM-22(20) catalyst. The conversion of DMF can be further increased up to 73% with 71% PX selectivity when using the MCM-22(15) catalyst. However, when the beta zeolites catalyzed DMF

conversion, the conversion of DMF was 11%, 15%, and 32% for beta-25, beta-50, and beta-100. All three beta zeolites exhibited significantly lower catalytic performance than MCM-22. Only 1% DMF conversion with 3% PX selectivity was obtained for the ZSM-5 catalyst under the same reaction conditions.

The acid density of ZSM-5 (608 µmol g^{-1}) is close to that of MCM-22 zeolites (Table 2), which suggests that the significant performance differences do not originate from the variation in the number of acid sites. The catalytic performance of beta was higher than that of ZSM-5, which was in line with a previous report.[7] This may be because the beta with 12-MR shows better mass transfer than the ZSM-5 with 10-MR. However, MCM-22 also contains 10-MR windows (0.40 nm × 0.55 nm) and 10-MR sinusoidal channels (0.41 nm × 0.51 nm), which suggests that the high catalytic performance may mainly result from the acid sites on the external surface. Besides, the S_{ext} of ZSM-5 and beta-50 were 91 and 133 m^2 g^{-1} (Table S1), which were comparable to those of MCM-22 zeolites. Therefore, the high catalytic performance of MCM-22 was not just due to the high external surface. Compared to ZSM-5 and beta, MCM-22 has a pocket
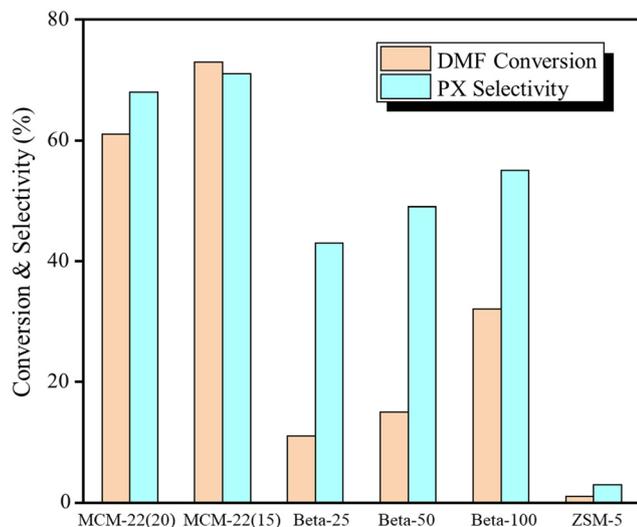
6182 | *Catal. Sci. Technol.*, 2025, **15**, 6179–6187

This journal is © The Royal Society of Chemistry 2025

Fig. 4 Catalytic performance of MCM-22(15), MCM-22(20), beta-25, beta-50, beta-100, and ZSM-5 for the D–A conversion of DMF (100 mg catalyst, AA/DMF = 2, 7.5 mmol DMF, 160 °C, N$_2$ 1.0 MPa, 5 h).

3.3 The origin of MCM-22 catalytic activity

Previous studies have revealed that when SiO$_2$ precursors with molecular size larger than the pore size of zeolites are employed, the SiO$_2$ predominantly deposits on the external surface.[34] To better understand the origin of high catalytic activity for MCM-22, TEOS with a molecular size (Fig. S4) exceeding the pore entrance of MCM-22 was selected as the SiO$_2$ precursor, enabling selective coverage of acid sites in MCM-22(15). As shown in Fig. 5a, the total acid density of MCM-22(15) decreased by 27% with the acid strength decreasing slightly after being modified by 15% SiO$_2$ (SiO$_2$/MCM-22(15)). When they were used as catalysts for the TPB isomerization reaction, the activity of SiO$_2$/MCM-22(15) was reduced by more than 85% compared to that of MCM-22(15) (Fig. 5b). Due to the molecular dimensions of TPB (Fig. S5) exceeding the micropore structure of MCM-22, the TPB isomerization reaction mainly occurred over the external acid sites.[29] The observed activity variations in TPB conversion directly correlate with the differential surface acid site concentrations between MCM-22(15) and SiO$_2$/MCM-22(15). The results of N$_2$ adsorption isotherms (Fig. S6 and Table S1) also demonstrated that the pore structure of MCM-22(15) was

retained after SiO$_2$ loading. Therefore, these results prove that SiO$_2$ mainly covers the acid sites on the external surface of MCM-22, which agrees with previous reports. Moreover, when MCM-22(15) and SiO$_2$/MCM-22(15) were used to catalyze the conversion of DMF, the difference in the activity had similar results to the isomerization reaction, which suggested that the active site of DMF conversion to PX was mainly from the acid sites on the external surface of the MCM-22.

To probe the contributions of B acid and L acid sites, DTB-Py with a molecular size (Fig. S7) exceeding the pore entrance of MCM-22 was introduced into the reaction system for selective deactivation of surface-exposed B acid centers in MCM-22.[33] Fig. 6 shows the effect of DTB-Py on the conversion of DMF and the yield of products in the reaction of DMF and AA into PX. The DMF conversion and PX yield were 64% and 38% over MCM-22(15) at 160 °C after 3 h. When a small amount of DTB-Py (the molar ratio of DTB-Py/DMF is 2 × 10^{-3}) was added to the reaction medium, both DMF conversion and PX yield decreased significantly to 38% and 22%, respectively. The conversion of DMF and the yield of PX decreased with the addition of DTB-Py, and they further decreased to only 16% and 6% when the ratio of DTB-Py/DMF was up to 10 × 10^{-3}. This indicated that the rate of DMF conversion to PX was mainly controlled by the B acid sites on the external surface of MCM-22. In addition, the yield of HDO obtained by DMF hydrolysis and DMBA formed by dehydrating the cycloadduct (Scheme S1) showed a similar trend to PX during the selective poison test, which implied that the DMF hydrolysis reaction was also catalyzed by B acid sites. However, the yield of DMCHO isomerized from oxanorbornene (Scheme S1) hardly changed with the addition of DTB-Py. Moreover, when pyridine (pyridine/DMF = 0.05) was used to simultaneously poison both B and L acid sites, the yield of DMCHO drastically decreased. Previous DFT study showed that L acids can lower the energy barrier of D–A cycloaddition, and B acids do not catalyze the cycloaddition.[13] Therefore, the D–A cycloaddition reaction might be catalyzed by L acid sites over MCM-22 zeolites.

In situ FTIR spectra were measured to further probe the D–A cycloaddition reaction process. MCM-22(15) was first dehydrated at 350 °C under vacuum conditions for 2 h and then cooled to 30 °C. As shown in Fig. 7, a strong terminal Si–OH group signal at 3745 cm^{-1} was observed, which was mainly caused by the external silanols (black line).[35] The peak of the bridging Si–OH–Al groups was also detected at ~3620 cm^{-1}.[36] The peak intensity of 3745 and 3620 cm^{-1}

Table 2 NH$_3$-TPD and Py-IR analytical data for MCM-22(15) and MCM-22(20)

Samples	Acid densities (μmol g^{-1})					Strong/weak	B/L	Si/Al^c
	Total acid^a	Weak acid^a	Strong acid^a	B acid^b	L acid^b			
MCM-22(15)	520	317	203	416	104	0.64	4.0	14.7
MCM-22(20)	447	300	147	254	194	0.69	1.3	19.6

^{a} Derived from deconvoluted NH$_3$-TPD curve analysis. ^{b} Evaluated through synergistic NH$_3$-TPD and Py-IR results. ^{c} Measured *via* ICP-OES.
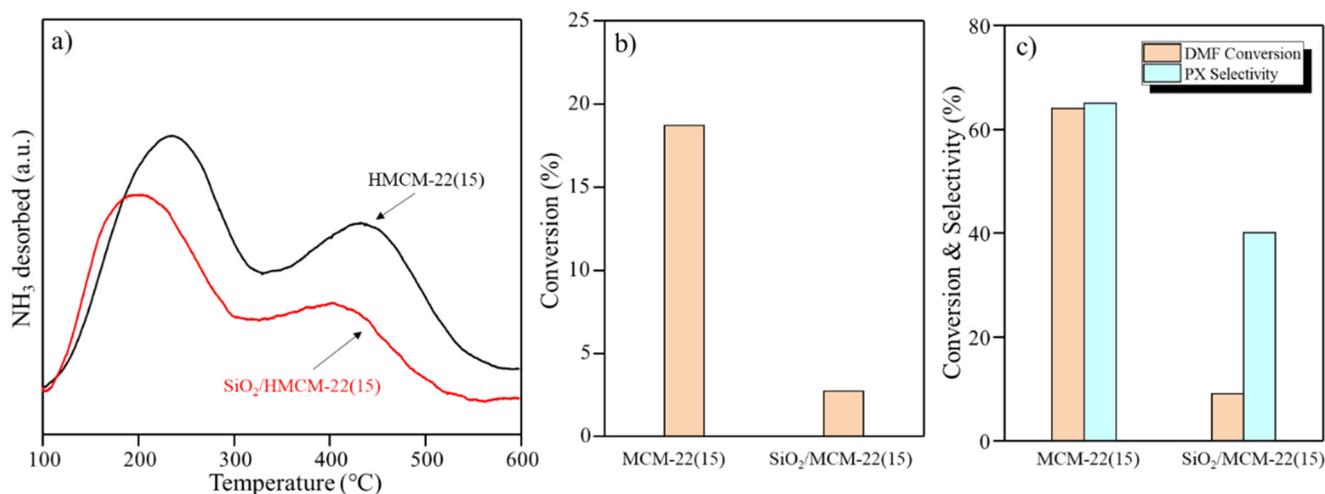
Fig. 5 (a) NH$_3$-TPD curves of MCM-22(15) and SiO$_2$/MCM-22(15). (b) The activity of TPB isomerization over MCM-22(15) and SiO$_2$/MCM-22(15) (reaction conditions: T = 320 °C, WHSV$_{TPB}$ = 1.7 min^{-1}, $W_{cat.}$ = 50 mg). (c) The conversion of DMF and selectivity of PX over MCM-22(15) and SiO$_2$/MCM-22(15) (100 mg catalyst, AA/DMF = 2, 7.5 mmol DMF, 160 °C, N$_2$ 1.0 MPa, 3 h).

decreased after the adsorption of DMF and AA at 30 °C (red line), suggesting that the reactants could be adsorbed at hydroxyl sites. Owing to the hydroxyl group of AA, the signal intensity at 3490 cm^{-1} was increased. The emergence of the alkyl stretching signal at 2875, 2925, and 2975 cm^{-1} was attributable to the C–H structure of DMF and AA. Interestingly, the peaks corresponding to the C–H stretching of benzene at 3110 and 3045 cm^{-1} were observed after adsorbing the reactants at 30 °C, meaning that DMF and AA were easily converted into PX or DMBA. The bridging intensity of Si–OH–Al groups exhibited a slight decrease with increasing temperature, which correlates with prior research demonstrating the catalytic role of B acid sites for the dehydration reaction.[12,13] Therefore, the decline in intensity of bridging Si–OH–Al groups was due to their participation in the reaction network. The intensity of the terminal Si–OH groups was slightly raised when the temperature increased to 160 °C, but it was still much lower than that before the adsorption of reactants. This result indicated that the external silanols interact strongly with the reactants. Almost no product could be detected when amorphous SiO$_2$ was employed to catalyze the D–A cycloaddition reaction. This verification confirms that Si–OH groups cannot directly catalyze the D–A cycloaddition reaction. Considering the location of external silanols at the pore entrance of the pocket structure, their adsorption of reactants could
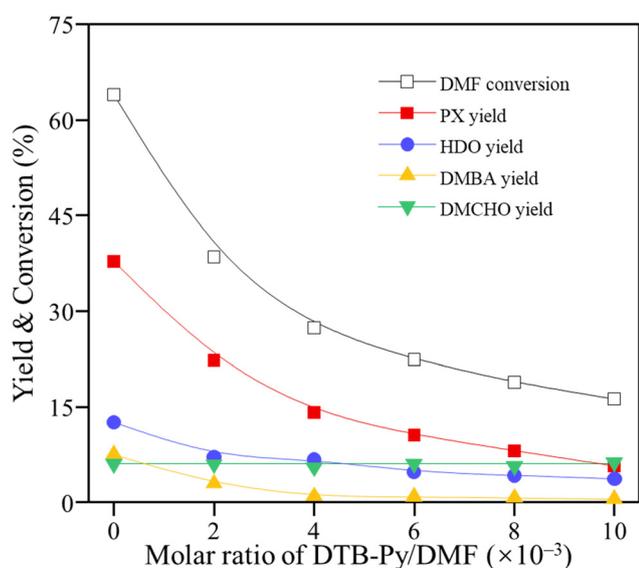

Fig. 6 The effect of DTB-Py on the DMF conversion and the product yield of MCM-22(15) (100 mg catalyst, AA/DMF = 2, 7.5 mmol DMF, 160 °C, N$_2$ 1.0 MPa, 3 h).
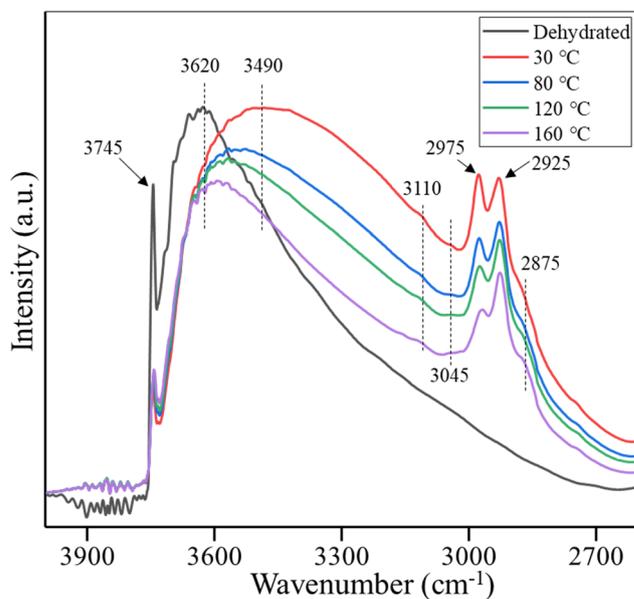

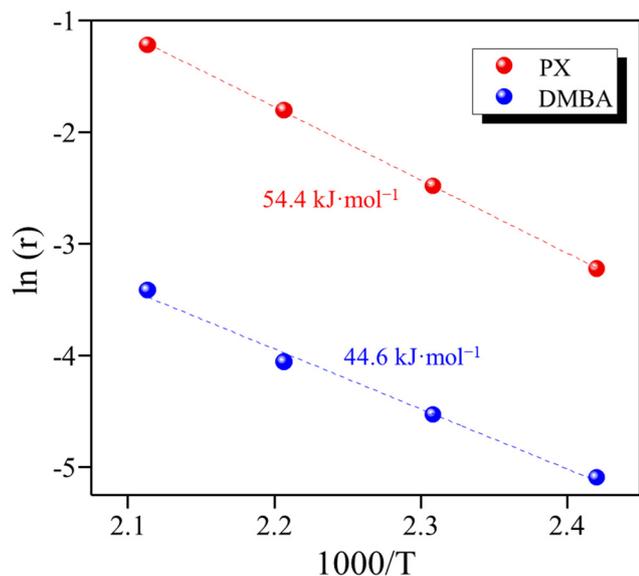**Fig. 7** The *in situ* FTIR spectra of MCM-22(15) under different conditions.

Fig. 8 Temperature-dependent kinetic profiling of PX and DMBA formation over MCM-22(15).

Apparent activation energies (E_a) for PX formation were further measured on each catalyst (Fig. 8 and S8). The E_a for PX formation over beta-100 and MCM-22 catalysts was found to be ~50 kJ mol^{-1}, approaching those previously reported for zeolites and other solid acid catalysts.[19,37] However, the E_a for PX formation over beta-25 and beta-50 catalysts was only 17.2 and 16.6 kJ mol^{-1}, respectively. Our previous findings demonstrated that when diffusion limitations are eliminated, the E_a for PX formation on beta zeolites was close to those of the beta-100 and MCM-22 catalysts.[12] Conversely, under strong diffusion limitations, E_a values decrease substantially while catalytic activity concurrently declines. This indicated that significant diffusion limitation existed during reactions over beta-25 and beta-50, while such effects were effectively eliminated in beta-100 and MCM-22 catalysts. For MCM-22 zeolite, the pocket structures can provide abundantly accessible acid sites, effectively avoiding mass transfer limitations. Beta-100 shows a higher mass transfer efficiency than beta-25 and beta-50 maybe because of its small particle size (Fig. S9). Moreover, the formation rate of PX per acid site was tested for MCM-22 and beta-100 zeolites under net kinetic control (Fig. S10). MCM-22 zeolites exhibited higher catalytic activity than beta-100, which further demonstrated their superior catalytic performance.

promote the D–A reaction at the active sites of the pocket structure.
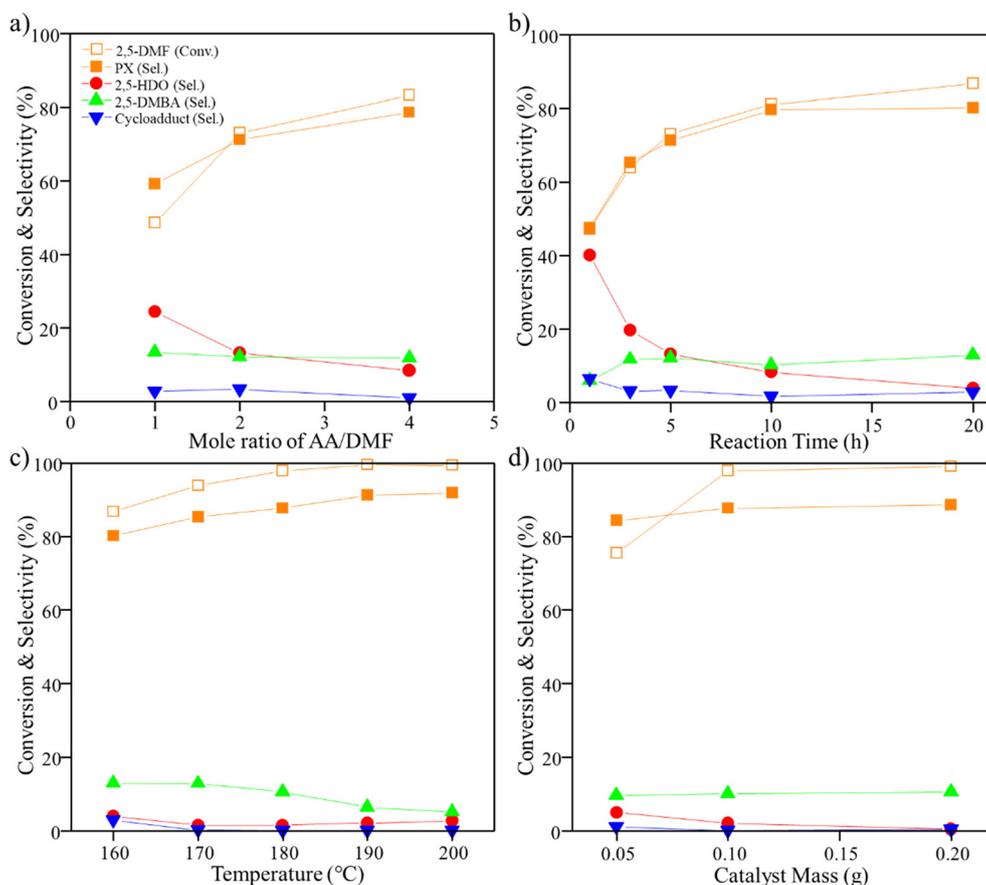

Fig. 9 The effect of (a) reactant molar ratio, (b) reaction time, (c) temperature, and (d) catalyst amount on catalytic performance over MCM-22(15). Reaction conditions: (a) 7.5 mmol DMF, T = 160 °C, p = 1.0 MPa N$_2$, t = 5 h, $W_{cat.}$ = 100 mg; (b) 7.5 mmol DMF, 15 mmol AA, T = 160 °C, p = 1.0 MPa N$_2$, $W_{cat.}$ = 100 mg; (c) 7.5 mmol DMF, 15 mmol AA, t = 10 h, p = 1.0 MPa N$_2$, $W_{cat.}$ = 100 mg; (d) 7.5 mmol 2,5-DMF, 5 mmol AA, t = 10 h, p = 1.0 MPa N$_2$, T = 190 °C.

Additionally, both MCM-22 and beta zeolites were employed in the D–A cycloaddition reaction of DMF and ethylene. The results indicated that MCM-22 showed relatively high catalytic activity (Fig. S11). However, the performance variations among zeolites differ from those observed in the reaction of DMF and AA. This discrepancy likely arises from the differential effects of zeolites on reaction processes, such as reactant diffusion and adsorption.

Besides, both PX and DMBA were formed through D–A cycloaddition and dehydration steps, but the E_a measured for DMF conversion to DMBA (44.6 kJ mol^{-1}) was found to be significantly lower than that required for PX production. A previous study demonstrated that the reaction of DMF to cycloadduct shows a low reaction energy barrier.[12] Fig. 6 shows that the DMBA and PX yields exhibited a marked dependence on B acid site density. These results suggested that the dehydration process was the limiting step, which agreed with our previous research. The E_a of DMF to DMBA is lower than that of PX, indicating that the cycloadduct is more easily dehydrated than oxa-norbornene. However, the selectivity of DMBA was lower than PX, which may be because the pores of zeolites can stabilize the oxa-norbornene intermediate that formed the PX.[30]

3.4 The influence of reaction parameters

The effects of reactant molar ratio, reaction duration, reaction temperature, and catalyst mass were researched to better understand the DMF conversion process. According to the data presented in Fig. 9a, both DMF conversion and PX selectivity exhibited a positive correlation with the elevation of AA/DMF molar ratios. The selectivity of by-products HDO, DMBA, and DMCHO decreased with increasing AA/DMF molar ratio. Therefore, the high AA/DMF molar ratio was conducive to the formation of PX. As expected, the conversion of DMF and the selectivity of PX increased as the reaction time increased (Fig. 9b). Similar to the results in Fig. 9a, a concomitant reduction in HDO selectivity was observed with progressive DMF conversion to PX, ascribed to the reversible nature of the DMF-to-HDO hydrolysis reaction (Scheme S1). When the reaction time exceeded 10 h, the conversion of DMF and the selectivity of PX increased only slightly. The plotting of catalytic performance *versus* temperature is shown in Fig. 9c. With the temperature range from 160 to 190 °C, the DMF conversion and PX selectivity increased as the reaction temperature, while the DMBA selectivity exhibited an opposite trend. Compared with DMBA, high temperature is more helpful to the generation of PX, which is in line with the Fig. 8 result. Fig. 9d shows that the conversion of DMF and selectivity of PX increased from 76% and 84% to 98% and 88% as the mass of the catalyst increased from 0.05 g to 0.1 g. When the mass of the catalyst further increased to 0.2 g, the conversion of DMF and selectivity of PX did not change significantly.

4. Conclusions

The MCM-22 zeolites have been demonstrated to show high catalytic performance in the D–A cycloaddition of DMF and AA to PX. The active site of DMF conversion to PX was mainly from the easily accessible acid sites at the pocket structure on the external surface of MCM-22. The rate of DMF conversion to PX was mainly controlled by the B acid sites on the external surface. The reactants could adsorb at the external silanol sites at the pore entrance of the pocket structure, which could also promote the D–A cycloaddition of DMF. These results not only help to understand the D–A conversion of DMF to PX but also provide a new perspective on the application of zeolites.

Conflicts of interest

There are no conflicts to declare.

Data availability

Supplementary information is available. See DOI: **https://doi.org/10.1039/D5CY00614G**.

The data supporting this article have been included as part of the SI.

References

1 L. Kumar, S. Asthana, B. L. Newalkar and K. K. Pant, *Catal. Rev.: Sci. Eng.*, 2022, 1–43, DOI: **10.1080/01614940.2022.2097641**.

2 N. Chakinala and A. G. Chakinala, *Ind. Eng. Chem. Res.*, 2021, **60**, 5331–5351.

3 B. Yan, J. Wu, X. S. Li, N. Liu, Q. X. Ma and B. Xue, *Catal. Lett.*, 2024, **154**, 2752–2760.

4 E. M. Gallego, M. T. Portilla, C. Paris, A. Leon-Escamilla, M. Boronat, M. Moliner and A. Corma, *Science*, 2017, **355**, 1051–1054.

5 M. W. N. Lobão, A. L. Alberton, S. A. B. V. Melo, M. Embiruçu, J. L. F. Monteiro and J. C. Pinto, *Ind. Eng. Chem. Res.*, 2011, **51**, 171–183.

6 S. Dutta and N. S. Bhat, *Biomass Convers. Biorefin.*, 2020, **13**, 541–554.

7 J. A. Mendoza Mesa, F. Brandi, I. Shekova, M. Antonietti and M. Al-Naji, *Green Chem.*, 2020, **22**, 7398–7405.

8 P. T. M. Do, J. R. McAtee, D. A. Watson and R. F. Lobo, *ACS Catal.*, 2012, **3**, 41–46.

9 R. Zhao, L. Wu, X. Sun, H. Tan, Q. Fu, M. Wang and H. Cui, *Microporous Mesoporous Mater.*, 2022, **334**, 111787.

10 Z. Ju, X. Yao, X. Liu, L. Ni, J. Xin and W. Xiao, *Ind. Eng. Chem. Res.*, 2019, **58**, 11111–11120.

6186 | *Catal. Sci. Technol.*, 2025, **15**, 6179–6187

This journal is © The Royal Society of Chemistry 2025

11 S. Sun, C. Fu, X. Yu, X. Yi, A. Zheng, Y. Gu and H. Shi, *J. Catal.*, 2024, **432**, 115418.

12 J. Huang, B. Yan, Z. Wang, X. Chen, Z. Liu and B. Xue, *Appl. Catal., A*, 2025, **691**, 120067.

13 N. Nikbin, P. T. Do, S. Caratzoulas, R. F. Lobo, P. J. Dauenhauer and D. G. Vlachos, *J. Catal.*, 2013, **297**, 35–43.

14 Y.-P. Li, M. Head-Gordon and A. T. Bell, *J. Phys. Chem. C*, 2014, **118**, 22090–22095.

15 C.-C. Chang, S. K. Green, C. L. Williams, P. J. Dauenhauer and W. Fan, *Green Chem.*, 2014, **16**, 585–588.

16 J.-C. Kim, T.-W. Kim, Y. Kim, R. Ryoo, S.-Y. Jeong and C.-U. Kim, *Appl. Catal., B*, 2017, **206**, 490–500.

17 X. Feng, Z. Cui, K. Ji, C. Shen and T. Tan, *Appl. Catal., B*, 2019, **259**, 118108.

18 J. McGlone, P. Priecel, L. Da Vià, L. Majdal and J. Lopez-Sanchez, *Catalysts*, 2018, **8**, 253.

19 C. L. Williams, K. P. Vinter, C.-C. Chang, R. Xiong, S. K. Green, S. I. Sandler, D. G. Vlachos, W. Fan and P. J. Dauenhauer, *Catal. Sci. Technol.*, 2016, **6**, 178–187.

20 F. N. Gu, F. Wei, J. Y. Yang, N. Lin, W. G. Lin, Y. Wang and J. H. Zhu, *Chem. Mater.*, 2010, **22**, 2442–2450.

21 R. Srivastava, *Catal. Today*, 2018, **309**, 172–188.

22 Z. Qin, W. Shen, S. Zhou, Y. Shen, C. Li, P. Zeng and B. Shen, *Microporous Mesoporous Mater.*, 2020, **303**, 110248.

23 J. H. Ahn, R. Kolvenbach, C. Neudeck, S. S. Al-Khattaf, A. Jentys and J. A. Lercher, *J. Catal.*, 2014, **311**, 271–280.

24 K. Egeblad, C. H. Christensen, M. Kustova and C. H. Christensen, *Chem. Mater.*, 2007, **20**, 946–960.

25 V. A. Ostroumova and A. L. Maksimov, *Pet. Chem.*, 2019, **59**, 788–801.

26 A. Schwanke and S. Pergher, *Appl. Sci.*, 2018, **8**, 1636.

27 M. E. Leonowicz, J. A. Lawton, S. L. Lawton and M. K. Rubin, *Science*, 1994, **264**, 1910–1913.

28 J. Chen, T. Liang, J. Li, S. Wang, Z. Qin, P. Wang, L. Huang, W. Fan and J. Wang, *ACS Catal.*, 2016, **6**, 2299–2313.

29 B. Yan, Y. Feng, Z. Liu and B. Xue, *Res. Chem. Intermed.*, 2024, **50**, 4301–4313.

30 V. J. Margarit, E. M. Gallego, C. Paris, M. Boronat, M. Moliner and A. Corma, *Green Chem.*, 2020, **22**, 5123–5131.

31 A. Al-Nayili and M. Albdiry, *J. Porous Mater.*, 2021, **28**, 1439–1448.

32 M. Hu, B. Zhao, D.-Y. Zhao, M.-T. Yuan, H. Chen, Q.-Q. Hao, M. Sun, L. Xu and X. Ma, *RSC Adv.*, 2018, **8**, 15372–15379.

33 Y. Huang, H. Zhang, L. Gao, T. Yan, Y. Yan, Y. Zhang and Y. Tang, *Microporous Mesoporous Mater.*, 2022, **341**, 112110.

34 H. Han, H. Yang, A. Zhang, L. Ren, X. Nie, C. Chen, M. Liu, C. Shi, C. Song and X. Guo, *Inorg. Chem. Front.*, 2022, **9**, 3348–3358.

35 A. Corma, C. Corell, V. Fornés, W. Kolodziejski and J. Pérez-Pariente, *Zeolites*, 1995, **15**, 576–582.

36 Y. Wu, F. Tian, J. Liu, D. Song, C. Jia and Y. Chen, *Microporous Mesoporous Mater.*, 2012, **162**, 168–174.

37 J. Y. Yeh, S. S. Chen, S. C. Li, C. H. Chen, T. Shishido, D. C. W. Tsang, Y. Yamauchi, Y. P. Li and K. C. W. Wu, *Angew. Chem., Int. Ed.*, 2021, **60**, 624–629.